

Incommensurate magnetic modulation in K-rich cryptomelane, $\text{K}_x\text{Mn}_8\text{O}_{16}$ ($x \approx 1.46$)

Liam A. V. Nagle-Cocco,^{*,†} Joshua D. Bocarsly,^{†,‡} Krishnakanth Sada^{a,¶},
Clemens Ritter,[§] Emmanuelle Suard,[§] Nicola D. Kelly^{b,†}, Cheng Liu,[†] Clare P.
Grey,[‡] Prabeer Barpanda,^{¶,||} and Siân E. Dutton^{*,†}

[†]*Cavendish Laboratory, University of Cambridge, Cambridge, CB3 0HE, United Kingdom.*

[‡]*Yusuf Hamied Department of Chemistry, University of Cambridge, Cambridge, CB2 1EW,
United Kingdom.*

[¶]*Faraday Materials Laboratory (FaMaL), Materials Research Centre, Indian Institute of
Science, C. V. Raman Avenue, Bangalore, 560012, India.*

[§]*Institut Laue-Langevin, 38042, Grenoble, France.*

^{||}*Helmholtz Institut Ulm (HIU), Electrochemical Energy Storage, Ulm 89081, Germany.*

E-mail: lavn2@cam.ac.uk; Email:sed33@cam.ac.uk

^aPresent address: Department of Materials Science, University of Oxford, Oxford, OX1 3PH, United Kingdom.

^bPresent address: Department of Chemistry, Inorganic Chemistry Laboratory, University of Oxford, Oxford, OX1 3QR, United Kingdom.

Abstract

Cryptomelane is a hollandite-like material consisting of K^+ cations in an $\alpha\text{-MnO}_2$ tunnel-like crystallographic motif. A sample with stoichiometry $\text{K}_{1.461(4)}\text{Mn}_8\text{O}_{16}$ has been synthesised and its magnetic properties investigated using variable-temperature magnetic susceptibility, heat capacity, and neutron powder diffraction. Three distinct magnetic transitions at 184 K, 54.5 K, and 24 K are assigned to $\text{K}_{1.461(4)}\text{Mn}_8\text{O}_{16}$.

Magnetic Bragg peaks emerge below 54.5 K, and from their positions they indicate a modulated magnetic structure which is incommensurate with the crystallographic nuclear structure. The model consistent with the data is a dual- \vec{k}_{mag} structure with a canted ferrimagnetic $\vec{k}_{\text{mag}} = 0$ component and an incommensurate $\vec{k}_{\text{mag}} = (0, 0, k_z)$ [$k_z = 0.36902(15)$] component, with the latter most likely to be of the helical type formerly proposed for this material. Below 24 K, there is a magnetic transition, which gives rise to a different set of magnetic Bragg peaks indicative of a highly complex magnetic structure.

Introduction

α -MnO₂ is a polymorph of MnO₂ comprised of corner-sharing rutile-like ribbons of MnO₆ octahedra which share edges to form a tunnel structure.¹ This structural motif has led to significant interest since in addition to doping within the MnO₂ framework,² it is possible to incorporate dopants into the tunnels. The magnetic properties are of interest because the Mn lattice is made up of multiple triangular units that give rise to a high degree of geometric frustration.^{3,4} α -MnO₂ is commonly studied in an X -doped form, $X_x\text{MnO}_2$ with X a large cation like K⁺, Ba²⁺, or Na⁺.^{1,5,6} In this work we focus on the K-doped variant, $\text{K}_x\text{Mn}_x^{3+}\text{Mn}_{8-x}^{4+}\text{O}_{16}$, which is a naturally-occurring mineral called cryptomelane, with mixed Mn valence depending on the level of doping. K ions can be incorporated into the tunnel structure to a maximum of $x = 2$, as shown in Figure 1(a), with the doping limited by the occupancy of K in the tunnels. Due to the large tunnels, cryptomelane has significant potential for various applications. For example, it can serve as the positive electrode in K-ion^{7,8} and Zn-ion⁹ batteries. Further, many studies have investigated the potential of the material for oxidising organic pollutants such as toluene and ethyl acetate.¹⁰⁻¹³

Cryptomelane has been studied extensively for its magnetic properties,¹⁴⁻²² which stem from its structure, which is prone to magnetic frustration. The frustration arises due to competition between the three neighbouring Mn-Mn magnetic interactions. These are J_1 :

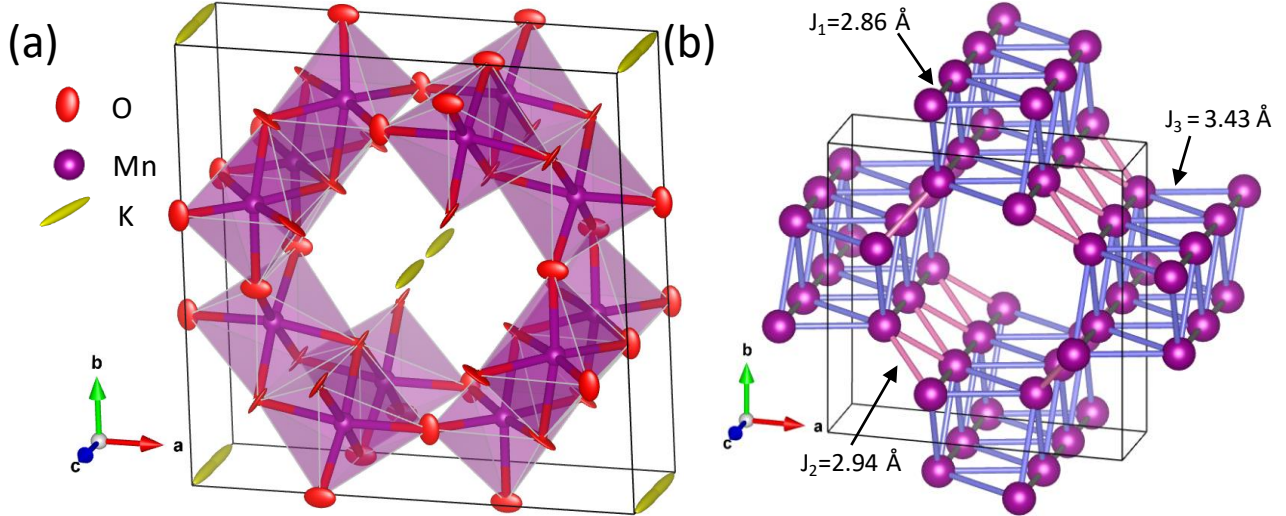


Figure 1: (a) Crystallographic structure of cryptomelane in the $I4/m$ space group, as viewed at a slight angle from the c -axis, with atoms displayed as ellipsoids of 95% probability. Red: O; purple: Mn; yellow: K. (b) The Mn lattice of cryptomelane only, showing the three nearest Mn-Mn interactions. Grey: J_1 , pink: J_2 , purple: J_3 .

interactions between edge-sharing MnO_6 octahedra where the Mn-Mn distance is parallel with the c -axis and the direction of the tunnels; J_2 : a second edge-sharing interaction between MnO_6 octahedra where the Mn-Mn interaction is approximately 29° from the ab -plane; and J_3 : corner-sharing MnO_6 octahedra, which are separated from one another by bond-angle $\theta_{\text{Mn-O-Mn}} \approx 130^\circ$. These are labelled schematically in Figure 1(b).

The magnetic properties of cryptomelane are found to be highly dependent on the value of K-stoichiometry, x , with quite different temperature-dependent magnetic behaviour in the range $0.72 < x < 1$ compared with $1 < x < 2$. For the lower x -range, short-range ferromagnetic or ferrimagnetic correlations occur along with formation of a spin glass, with transition reported in the range $33.1 < T_g(\text{K}) < 50$.^{15,18,19} In this work, we focus on the higher- x compositional range, where there are multiple magnetic transitions and a lack of consensus on their origin.^{16,17,19–22} The majority of studies of the magnetic structure of cryptomelane with $x \geq 1$ report two magnetic transitions, one at $T \approx 55 \text{ K}$ and another in the range $20 - 25 \text{ K}$. In some works, a higher temperature transition observed by magnetisation and electrical transport measurements, occurring in the range $180 < T(\text{K}) < 250$, is

assigned to charge ordering of Mn^{3+} and Mn^{4+} .^{17,19} No associated superstructure has thus far been reported by diffraction. Based on magnetic susceptibility measurements, the transition at $T \approx 50$ K is described as having non-collinear AFM ordering, helical magnetism or weak ferromagnetism.^{17,19–21} Single crystal studies^{16,17} involving isothermal magnetisation measurements show that there is significant anisotropy and irreversibility when the field is applied perpendicular to the tunnels, indicating a net moment in the ab -plane. Below the lower temperature transition at $T \approx 20$ K literature reports formation of a spin-glass-like or helical order. This is based on observed frequency-dependence of transition temperature in AC susceptibility and divergence between temperature-dependent susceptibility during cooling in the presence/absence of a magnetic field. Additionally, the spin-glass-like state is believed to relate to observed magnetic memory behaviour,^{21,22} in which holding the material at a particular temperature in a magnetic field during cooling leads to features at that temperature during subsequent heating.²² A prior neutron diffraction study on a sample of $\text{K}_{1.72}\text{Mn}_8\text{O}_{16}$ observed a different set of magnetic Bragg peaks in each temperature regime;²³ the authors do not solve the magnetic structure, but do suggest an incommensurate magnetic structure in the higher temperature regime and a commensurate magnetic structure below ~ 25 K. Besides this, no neutron diffraction experiments have so far explored the long-range magnetic order in cryptomelane of any stoichiometry, although a study on the Ba-analog²⁴ has found modulated magnetism, commensurate with the unit cell.

In this work, we present the first magnetic structure solution from a neutron diffraction study on a sample of cryptomelane, with stoichiometry $\text{K}_{1.461(4)}\text{Mn}_8\text{O}_{16}$ and average Mn oxidation state of approximately +3.82. Our results are compared to the theory, developed by Sato *et al.*^{16,17} in which simultaneous charge- and spin-modulations give rise to a helical ordering with a net moment. We find evidence in favour of this helical ferrimagnetism below 54.5 K. Furthermore, we observe the persistence of magnetic Bragg peaks below the proposed glass transition at 24 K, albeit at different positions compared with above the transition. This persistence of long-range magnetic order is inconsistent with prior reports

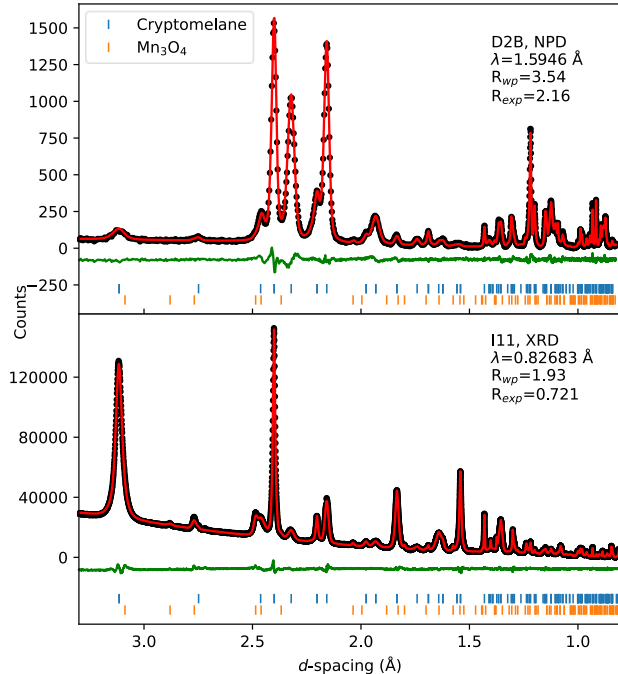


Figure 2: Experimental (black points) and calculated (red line, modeled by combined Rietveld refinement) diffraction data at room temperature for synchrotron XRD (bottom) and neutron diffraction (top). The difference between the model and data is shown in green. Blue tick-marks indicate nuclear Bragg peaks due to cryptomelane $\text{K}_{1.461(4)}\text{Mn}_8\text{O}_{16}$, and orange tick-marks indicate nuclear Bragg peaks due to the Mn_3O_4 impurity (3.54(3)% by weight). The R_{wp} and R_{exp} of the total refinement were 1.96 and 0.766 respectively (to 3 significant figures).

of a bulk spin-glass-like state.

Methods

Sample preparation. Cryptomelane was prepared, in a quantity of several grams, using a solid-state synthesis route with a target composition of $\text{K}_{1.33}\text{Mn}_8\text{O}_{16}$. The precursors in the molar ratio of 1.33:8 KNO_3 to MnCO_3 (99.994% and 99.9% purity respectively; both from Alfa Aesar) were mixed thoroughly using agate mortar and pestle, with a 5% molar excess of KNO_3 to account for K-loss during high-temperature calcination. Planetary mixing in ethanol was carried out for ~ 15 minutes. The resultant powder was annealed in air at 500°C for ~ 4 hours, with a heating rate of 5°C min^{-1} . Samples were cooled to room temperature

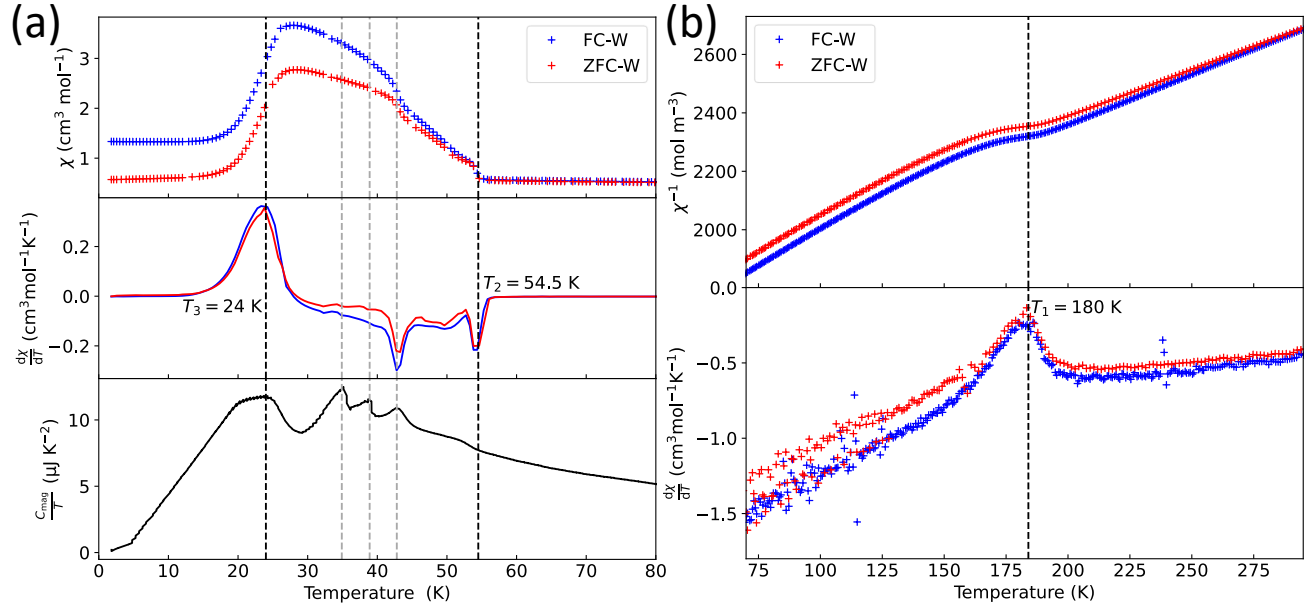


Figure 3: (a) Magnetic susceptibility χ , $d\chi/dT$, and heat capacity as a function of temperature. (b) Inverse magnetic susceptibility and $d\chi/dT$ as a function of temperature in the vicinity of T_1 . Vertical dashed lines indicate where transition temperature values are assigned; black lines are due to cryptomelane and grey lines are due to Mn_3O_4 .^{25–28} ZFC-W and FC-W denote zero-field-cooled and field-cooled measurements, measured during warming in a field of 200 Oe.

by switching off the furnace.

Magnetisation measurements. A Quantum Design Magnetic Properties Measurement System (MPMS-3) was used for DC susceptibility and isothermal magnetisation measurements. Measurements were taken during warming after cooling in zero field (ZFC-W) and in the measuring field (FC-W), where the measuring field was 200 Oe. Isothermal magnetisation measurements were performed in an external magnetic field between ± 70 kOe.

A Quantum Design 9 T Physical Properties Measurement System (PPMS) using the ACMS-II option was used for AC susceptibility. Measurements were taken with an AC driving field of 10 Oe in a static field of 10 Oe at 500 Hz, 1001 Hz, 1501 Hz, 2002 Hz, and 4004 Hz.

Heat capacity. A Quantum Design PPMS was used for heat capacity measurements. As is common for thermally insulating samples^{29–33} the sample was mixed with silver powder (Alfa Aesar, 99.99%, -635 mesh) in a 1:1 mass ratio to increase the conductivity; this was accounted for using tabulated T-dependent heat capacity of silver from Ref. 34. Apiezon N grease was used to provide thermal contact between the sample platform and the pellet. The lattice contribution to the heat capacity was estimated and accounted for using a Debye temperature³⁵ $T_D = 465.5$ K (see Figure S2 of Supplementary Information).

Diffraction. Room temperature X-Ray Diffraction (XRD) was performed using the I11 instrument^{36,37} on the synchrotron at Diamond Light Source ($\lambda = 0.82683$ Å) using the Mythen-2 position-sensitive detector, with a sample collection time of ~ 20 seconds. The sample was contained in a 0.5 mm diameter glass capillary, sealed with epoxy (Loctite Double Bubble). Low-temperature laboratory XRD was performed using a Bruker D8 Discover diffractometer (Cu $K\alpha$; $\lambda = 1.541$ Å), with an Oxford Cryosystems PheniX stage.

Constant-wavelength neutron diffraction experiments were performed at the Institut Laue-Langevin. Measurements were performed on the D2B (room-temperature; $\lambda = 1.5946$ Å) and D20 (2.5 K, 40 K, 44 K, 47 K, and 60 K; $\lambda = 2.4108$ Å) instruments. Both neutron and x-ray measurements were performed on aliquots of the same sample.

Diffraction analysis. Structural diffraction data were analysed using the software package TOPAS 5³⁸ using combined Rietveld refinement³⁹ of the room temperature I11 and D2B data. The background was fitted by a Chebyshev polynomial (order 15 and 6 for synchrotron data and neutron data respectively). A fixed TCHZ peak-shape refined from standard Si data was used⁴⁰ for the instrumental contribution to the synchrotron data, and the sample contribution to the peak-shape was accounted for using the Stephens peak type for anisotropic microstrain broadening⁴¹ convoluted with a Lorentzian particle size broadening function. The neutron peak shape was modeled using a convolution of the Stephens peak shape and Lorentzian and Gaussian particle size functions. Peak asymmetry was accounted for us-

ing a simple axial divergence model. All atomic positions, lattice parameters, and atomic displacement parameters were refined within symmetry constraints. Anisotropic atomic displacement parameters (ADPs)⁴² were refined for K and O, whereas isotropic thermal ADPs were used for Mn. Mn occupancies were fixed to 100% while all K and O occupancies were initially refined. The O2 site was fully-occupied within error, and so was fixed at 100% for the final refinement.

Magnetic diffraction analysis was performed using FULLPROF,⁴³ which we confirmed gives consistent results to TOPAS 5. Diffraction difference patterns were calculated by subtracting the neutron 60 K dataset from lower-temperature diffraction patterns using LAMP.⁴⁴ Candidate magnetic propagation vectors (\vec{k}_{mag}) were found using K Search, a tool in FULLPROF, using the position of peaks in the difference pattern. Precise values of parameters in \vec{k}_{mag} were refined against the difference pattern by Le Bail refinement.⁴⁵ BASIREPS^{46,47} was used to calculate the Irreducible Representations (IRs) for a given \vec{k}_{mag} (see Section I of Supplementary Information). For each IR with a set of i basis vectors, ψ_i , the components C_i are constrained appropriately based on the symmetry of the basis vector.

In FULLPROF, the March-Dollase model⁴⁸ was used to account for preferred orientation in the sample used for low-temperature neutron diffraction due to slightly non-spherical particle shape (see Figure S1 of Supplementary Information).

Results

Structural characterisation

The room temperature structure of cryptomelane, $\text{K}_x\text{Mn}_8\text{O}_{16}$, was investigated by neutron and x-ray diffraction on the D2B instrument at the ILL and the I11 instrument at Diamond Light Source, respectively. Combined Rietveld refinement was carried out with the previously-reported $I4/m$ (space group #87) structure.⁴⁹ In this tetragonal symmetry structure, there is a single Mn site, $8h(x, y, 0)$, and two inequivalent oxygen sites both at $8h(x,$

Table 1: The crystallographic parameters of cryptomelane at room temperature, as obtained by a combined Rietveld refinement of XRD data from the I11 instrument and neutron diffraction using the D2B instrument. Mn and O2 occupancies were fixed at 1.

Space group	$I4/m$
$a = b / \text{\AA}$	9.84955(10)
$c / \text{\AA}$	2.86234(16)
$V / \text{\AA}^3$	277.686(16)
χ^2	6.57
R_{wp}	1.96
R_{exp}	0.766
wt% Mn_3O_4	3.54(3)
K at $4e(0, 0, z)$	
$z(\text{K})$	0.368(11)
$U_{11} / \text{\AA}^2$	0.0283(13)
$U_{33} / \text{\AA}^2$	0.083(4)
occupancy(K)	0.368(11)
Mn at $8h(x, y, 0)$	
$x(\text{Mn})$	0.3499(4)
$y(\text{Mn})$	0.1650(5)
$B_{iso} / \text{\AA}^2$	0.545(6)
O at $8h(x, y, 0)$	
$x(\text{O1})$	0.1554(3)
$y(\text{O1})$	0.2024(2)
$U_{11}(\text{O1}) / \text{\AA}^2$	0.0038(18)
$U_{22}(\text{O1}) / \text{\AA}^2$	0.0085(17)
$U_{33}(\text{O1}) / \text{\AA}^2$	0.0002(8)
$U_{12}(\text{O1}) / \text{\AA}^2$	0.0073(14)
occupancy(O1)	0.953(3)
$x(\text{O2})$	0.5426(3)
$y(\text{O2})$	0.1637(4)
$U_{11}(\text{O2}) / \text{\AA}^2$	0.0082(10)
$U_{22}(\text{O2}) / \text{\AA}^2$	0.0146(10)
$U_{33}(\text{O2}) / \text{\AA}^2$	0.0065(8)
$U_{12}(\text{O2}) / \text{\AA}^2$	0.0038(9)
Bond lengths	
Mn-Mn (J_1 ; x 2) / \AA	2.86234(16)
Mn-Mn (J_2 ; x 2) / \AA	2.9380(8)
Mn-Mn (J_3 ; x 4) / \AA	3.4326(6)
Mn-O1 (x 1) / \AA	1.9556(17)
Mn-O1 (x 2) / \AA	1.9352(8)
Mn-O2 (x 1) / \AA	1.8904(16)
Mn-O2 (x 2) / \AA	1.8918(10)
Mn-O-Mn bond angles	
Mn-O1-Mn / $^\circ$	98.07(6)
Mn-O2-Mn / $^\circ$ 9	98.30(7)

$y, 0$). K is located within the tunnels in a partially occupied site, $4e(0, 0, z)$.

Structural parameters and refinement R-factors from a combined Rietveld refinement on the room temperature x-ray and neutron diffraction data are shown in Table 1, with the refined and calculated profile shown in Figure 2. These measurements indicate the presence of a 3.54(3)% (by weight) Mn_3O_4 impurity phase ($I4_1/amd$ space group, #121). Refinement of K site occupancy gives $x = 1.461(4)$ in $\text{K}_x\text{Mn}_8\text{O}_{16}$, with the excess K, as compared with the target composition of $\text{K}_{1.33}\text{Mn}_8\text{O}_{16}$, likely a consequence of the formation of the K-free Mn_3O_4 phase and the use of excess K during synthesis. The room-temperature Rietveld-refined crystallographic model is consistent with the reported crystal structure for cryptomelane.

In the Rietveld fit, anisotropic strain was implemented using Stephens' function.⁴¹ Refined strain parameters obtained from the synchrotron data, $S_{004} = 2740(60)$ a.u. and $S_{400} = 1598(9)$ a.u., show the anisotropic nature of this strain. Additionally, refinement of thermal ADPs using an anisotropic function showed that the thermal parameters of K^+ cations are highly anisotropic, with the $U_{33} = 0.083(5) \text{ \AA}^2$ several times larger than $U_{22} = U_{11} = 0.0283(13) \text{ \AA}^2$, as shown in Figure 1(a). The high degree of anisotropy in the K^+ ADPs could be due to either static disorder from K^+ ions occupying a range of $4e(0, 0, z)$ or due to dynamic disorder from K^+ hopping between adjacent sites.

The local environments of the two oxygen sites, O1 and O2, are different. O1 oxygen sites share bonds with K and Mn, and occur as the shared vertices of edge-sharing MnO_6 octahedra, whereas O2 oxygen sites are further from K than O1, and are the shared vertices of three corner-sharing MnO_6 octahedra. The ADPs for these two oxygen sites show different behaviour, likely resulting from the different degrees of freedom due to this MnO_6 connectivity. Refinement of site occupancies for oxygen indicated oxygen vacancies on one of the two O sites, with a refined occupancy on the O1 site of 0.953(3). This corresponds to $\text{K}_{1.461(4)}\text{Mn}_8\text{O}_{15.624(24)}$ and an average Mn oxidation of 3.72+. We will use the nominal oxygen content in all further discussions.

The MnO_6 octahedra are all identical. They exhibit four different Mn-O bond lengths between 1.8904(16) Å and 1.9556(17) Å. These bond length values and multiplicity are not consistent with a coherent static Jahn-Teller distortion (as compared with $\text{LaMn}^{3+}\text{O}_3$, see Ref. 50), although the bond length distortion may be in part the result of averaging multi-valent MnO_6 octahedra, some of which contain Jahn-Teller-active Mn^{3+} . The bond-length distortion index,⁵¹ D , is a physical parameter which is often used^{32,52-54} to quantify the degree of bond length distortion of coordinated species around a central ion. It is defined in Section VI of Supplementary Information. We here calculate a $D^{\text{Mn-O}} = 0.01322(14)$, which is similar to that previously reported for mixed $\text{Mn}^{3+/4+}\text{O}_6$ (with an average oxidation state of $\sim 3.42+$) in Ref. 53 for $\text{Pb}_3\text{Mn}_7\text{O}_{15}$.

Magnetometry and heat capacity

The magnetic transitions in our sample of $\text{K}_{1.461(4)}\text{Mn}_8\text{O}_{16}$ cryptomelane were studied using DC and AC magnetic susceptibility, heat capacity and isothermal magnetisation. We observe each of the three transitions which have previously been observed in K-rich cryptomelane. Here we follow the notation of Ref. 17, labelling the transitions as T_1 , T_2 , and T_3 in descending order of temperature.

Figure 3(a) shows T_2 and T_3 in the magnetic susceptibility χ , $\frac{d\chi}{dT}$, and magnetic heat capacity as a function of temperature, and Figure 3(b) shows T_1 in the inverse magnetic susceptibility and $\frac{d\chi}{dT}$. The precise values assigned to these transitions are determined from the plot of $\frac{d\chi}{dT}$ against temperature: $T_1 = 184$ K, $T_2 = 54.5$ K, and $T_3 = 24$ K. Consistency with heat capacity data justifies our use of $\frac{d\chi}{dT}$ for defining the transition temperatures. The other transitions observed in the heat capacity and magnetic susceptibility at 34.9 K, 38.9 K, and 42.8 K are all associated with magnetic ordering of Mn_3O_4 as has been described in the literature.²⁵⁻²⁸

The value of T_1 at 184 K, occurs within the range of previously-reported values.^{17,19} Previous reports^{17,19} have ascribed this transition to charge ordering of Mn^{3+} and Mn^{4+} ,

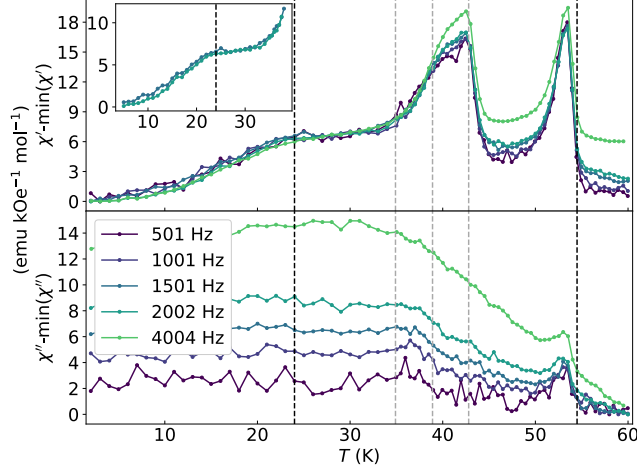


Figure 4: Variable -temperature and -frequency AC susceptibility measurements at 501 Hz, 1001 Hz, 1501 Hz, 2002 Hz, and 4004 Hz, shown in terms of the real χ' (top) and imaginary χ'' (bottom) components of the overall AC susceptibility. The inset shows the data for 1501 Hz and 2002 Hz only, with a focus on the T_3 transition. Positions of vertical lines match those in Figure 3.

which has also been observed in birnessite,⁵⁵ however no changes in the crystal structure have been observed here. Variable temperature XRD on our sample shows no evidence for a superstructure nor changes in the symmetry or discontinuities in the lattice parameters on cooling through this transition (see Figure S4 of Supplementary Information). Neutron diffraction experiments with lower wavelength to allow for a complete structural refinement are required to explore this possibility further.

Reported values of T_2 and T_3 vary over a broad range. Our values of $T_2 = 54.5$ K and $T_3 = 24$ K are slightly higher than most previous studies. For T_2 , Barudžija *et al.* report a T_2 transition of either 49 K or 51 K (sample-dependent)²¹ and Sato *et al.* report 52 K.¹⁷ For T_3 , these works report 21 K or 20 K, and 20 K respectively. This may be due to our defining the transition by the maximum in $\frac{d\chi}{dT}$, rather than the peak in the $\chi(T)$. Additionally, although there is ostensibly a very similar K^+ content, our work calculated K^+ content based on Rietveld refinement whereas the referenced works^{17,21} calculate K^+ content based on ratio of precursors. Consequently, there may be a discrepancy in stoichiometry. A theoretical study³ shows a dependence of transition temperature on the degree of K^+

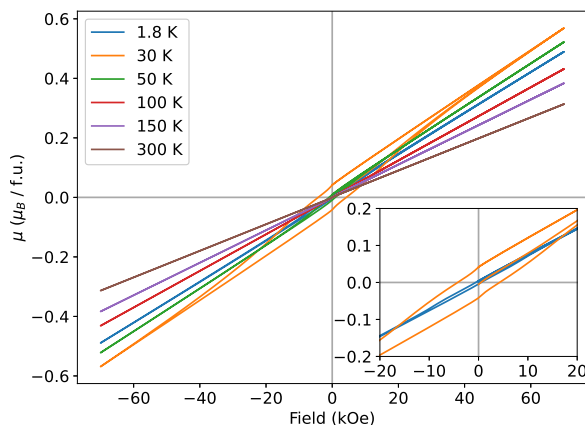


Figure 5: Fixed-temperature field-dependent magnetisation measurements at 1.8 K, 30 K, 50 K, 100 K, 150 K, and 300 K, showing moment per formula unit of $\text{K}_{1.461(4)}\text{Mn}_8\text{O}_{16}$. Inset: 1.8 K and 30 K field-dependent magnetisation data, zoomed in to highlight the different hysteretic behaviour.

cation content, and so it is unsurprising that the range of reported temperatures is fairly broad. In our sample, there is divergence between measurements performed after cooling with/without an external magnetic field (FC-C/ZFC-C, respectively), which has previously been interpreted as evidence of spin-glass-like ordering;^{21,22} this divergence is present at all measured temperatures (below 300 K) but becomes significant below T_2 .

AC susceptibility measurements between 2 K and 60 K are presented in terms of their real χ' and imaginary χ'' components in Figure 4. T_2 manifests as a large feature in both the real and imaginary susceptibility data, peaking around 53.5 K; this has been reported by Barudžija *et al.*^{21,22} in AC studies on K_xMnO_2 with similar composition. There is a more subtle shoulder for T_3 in our AC χ' , but no feature can be resolved for χ'' . Additionally, the incommensurate ordering of Mn_3O_4 around 43 K is present in our data as a large feature in χ' .

Finally, isothermal DC susceptibility measurements are shown in Figure 5. At 1.8 K, there is negligible hysteresis, suggesting there is no ferro- or ferri-magnetic behaviour for $T < T_3$. However, at 30 K and, to a lesser extent, 50 K, there is magnetic hysteresis. This suggests that for $T_3 < T < T_2$ there is a ferro- or ferri-magnetic component to the magnetic

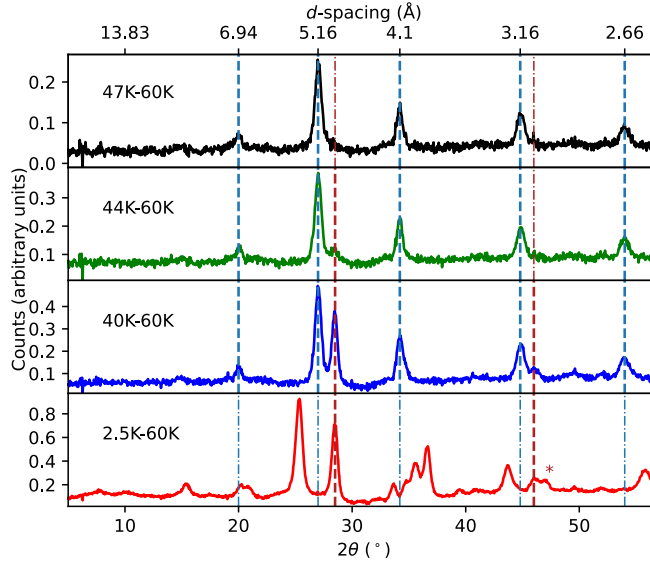


Figure 6: Experimental diffraction difference patterns i K-60 K ($i=47$ K, 44 K, 40 K, and 2.5 K). Blue dashed vertical lines indicate peaks associated with the commensurate $\vec{k}_{\text{mag}} = 0$ and incommensurate $\vec{k}_{\text{mag}} = (0, 0, \sim 0.37)$ components for $T_3 < T < T_2$. Dark red dashed vertical lines and asterisks show peaks associated with magnetic ordering in Mn_3O_4 . The vertical lines are thick at the temperatures where the associated peaks are present, and thin at temperatures where they are not.

structure. This is consistent with the previous reports.^{17,23}

Neutron diffraction: $T_3 < T < T_2$

Variable temperature neutron diffraction was measured on the D20 instrument at ILL, Grenoble [SI Figure S3]. Measurements were collected in the range 2.5 K to 60 K in order to study the changes on cooling through T_2 and T_3 . Difference patterns are shown in Figure 6, in which the diffraction data at 60 K (with no magnetic diffraction peaks) are subtracted from the lower-temperature diffraction patterns, to allow magnetic Bragg peaks to be readily identified. The changes in lattice parameters are continuous over the measured temperature points, and all lattice parameters decrease with cooling. The emergence of new peaks in neutron diffraction below $T_2 = 54.5$ K are consistent with magnetic ordering. Above $T \approx 40$ K, these could all be assigned to magnetic order below T_2 in cryptomelane, but in the diffraction measurement at 40 K, an additional magnetic Bragg peak due to magnetic ordering in the

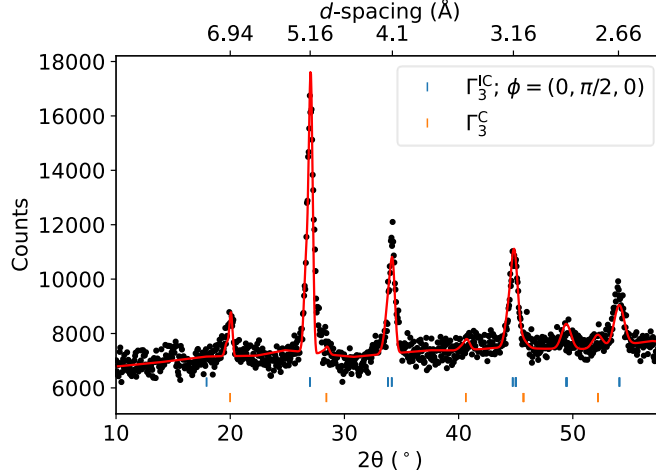


Figure 7: Experimental difference pattern 47 K-60 K, compared with calculated pattern. The calculated pattern was obtained by Rietveld refinement of the model for $T_3 < T < T_2$, consisting of a commensurate $\vec{k}_{\text{mag}} = 0$ and incommensurate $\vec{k}_{\text{mag}} = (0, 0, \sim 0.37)$ component. The incommensurate structure was represented with a helical model, with moments in the ab -plane.

Mn_3O_4 impurity is observed at $d = 4.9 \text{ \AA}$.

Indexing of the magnetic cell of cryptomelane $T_2 < T < T_3$ could not be carried out using a single propagation vector and instead 2 vectors, one commensurate and one incommensurate, were required. These were $\vec{k}_{\text{mag}} = (0, 0, 0)$ and $\vec{k}_{\text{mag}} = (0, 0, k_z)$ [$k_z = 0.36902(15)$]. Only one of the main magnetic peaks, at $d = 6.95 \text{ \AA}$, is assigned to the commensurate magnetic structure. This peak corresponds to the nuclear $[110]$ Bragg peak. As neutrons scatter from magnetic moment perpendicular to the scattering direction, this peak indicates that the magnetic moments are along a direction perpendicular to this vector, with the most likely by the symmetry of the crystallographic unit cell being either the $[001]$ or $[\bar{1}10]$ directions. Previous work on $\text{K}_{1.5}(\text{H}_3\text{O})_x\text{Mn}_8\text{O}_{16}$ single crystals indicates the magnetic hysteresis is much stronger in the ab -plane than along the c direction,¹⁷ which suggests that the moment is along $[\bar{1}10]$. The remaining four peaks ($d = 5.15, 4.10, 3.15, 2.65 \text{ \AA}$) can only be indexed to a propagation vector incommensurate with the crystal structure, $\vec{k}_{\text{mag}} = (0, 0, \sim 0.37)$.

For each propagation vector, there are multiple symmetry-allowed IRs. The correct IR would describe the basis vector behaviours at each magnetic site, which collectively

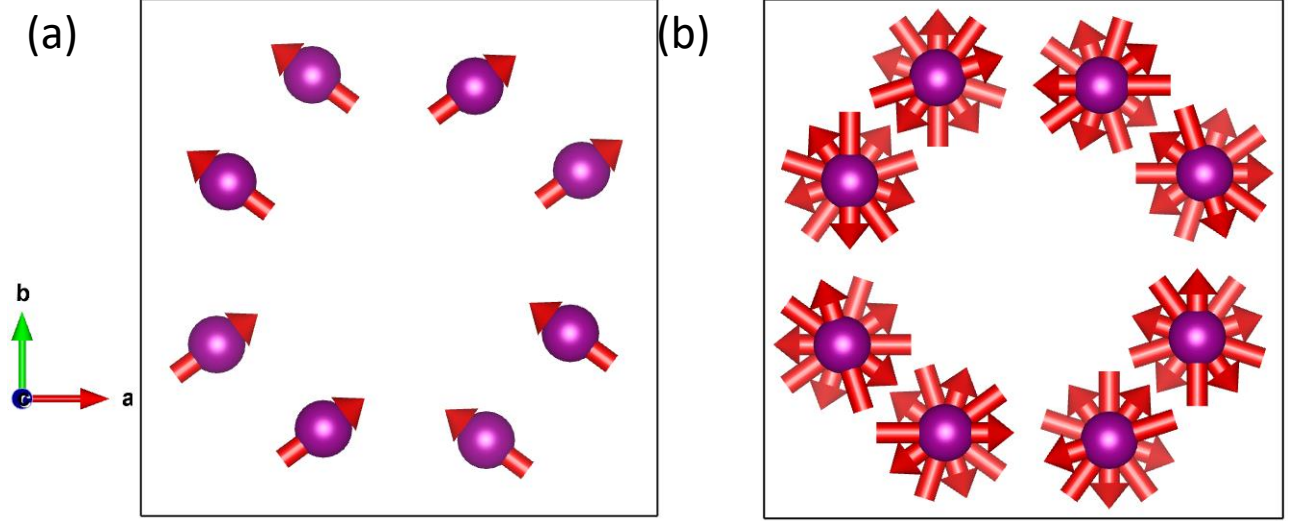


Figure 8: The refined magnetic unit cell for the (a) commensurate $\vec{k}_{\text{mag}} = (0, 0, 0)$ and (b) incommensurate $\vec{k}_{\text{mag}} = (0, 0, 0.37)$ components of the magnetic structure for $T_3 < T < T_2$. In (b), we assume the modulated magnetism is helical, with the moment entirely within the *ab*-plane.

make up the magnetic structure. There are 4 IRs for $\vec{k}_{\text{mag}} = (0, 0, \sim 0.37)$ and 6 IRs for $\vec{k}_{\text{mag}} = (0, 0, 0)$; these are denoted using Γ_i^j ($i = 1, 2, 3, 4, 5$, or 6 ; $j = \text{IC}$ or C where IC/C stands for InCommensurate or Commensurate). The coefficients C_i for the basis vectors ψ_i are tabulated in Section I of Supplementary Information.

We use magnetic Rietveld refinement to test the IRs against the experimental difference pattern (47 K-60 K), shown in Figure 7 and determine the magnetic structure. There are two IRs for the commensurate $\vec{k}_{\text{mag}} = (0, 0, 0)$ component which successfully fit the data: Γ_1^{C} , with a single basis vector ψ_1 , and Γ_3^{C} with four basis vectors and the constraints $C_1 = C_4$ and $C_2 = C_3$. The refined unit cell for Γ_1^{C} consists of ferromagnetically-aligned Mn spins along the *c*-axis. A net moment along *c* is inconsistent with field-dependent magnetisation measurements on single crystals¹⁷ and so Γ_1^{C} is not considered further. The refined magnetic structure for Γ_3^{C} is more complicated, and is shown in Figure 8(a). It breaks the C_4 rotational symmetry of cryptomelane in the *ab*-plane, with the *a* and *b* directions no longer equivalent. From the determined magnetic structure in Figure 8, J_1 and J_3 are both ferromagnetic, with moments parallel with each other. The J_2 interaction is more complex with ferromagnetic

correlations along b but antiferromagnetic correlations along a . Overall, each moment has its largest component in the a direction, but this component is cancelled such that there is no net moment along a , $m_a = 0$. Each spin is canted in the ab -plane away from the a direction towards the b -axis, resulting in a net moment $m_b > 0$; the canting angle is around 38° at 47 K but increases to around 45° at a lower temperature of 40 K. Γ_3^C resembles a model (called “C2-AFM” in their work) proposed in theoretical work using Ising spins,³ but with a spin canting in the [010] direction.

For the incommensurate $\vec{k}_{\text{mag}} = (0, 0, 0.37)$, it is possible to obtain a reasonable fit to the incommensurate peaks in the experimental diffraction data with Γ_i^{IC} ($i=2,3,4$) for several different models. The best fit is obtained with a helical model in which there is a constant moment in the ab -plane and a sinusoidally oscillating moment in the c -direction, which is slightly better than a similar fit with only the helical component in the ab -plane. These are obtained using Γ_3^{IC} and Γ_4^{IC} , with phase shifts applied in certain crystallographic directions; these are detailed further in Section I of Supplementary Information. Γ_2^{IC} can also be used to fit the data, but with lower quality than Γ_3^{IC} and Γ_4^{IC} .

Given the correspondence with theoretical⁴ and experimental^{16,17} works, we assume the structure is this ab -helical model, in which there are no moments in the c -axis and the moment is constant and rotating within the ab -plane. The Rietveld refinement at 47 K using the ab -helical model in conjunction with Γ_3^C is shown in Figure 7, and the associated magnetic structure is shown in Figure 8(b).

We have explored the possibility of magnetic phase segregation into two phases each with one of these two IRs, by varying the relative scale factors, S_C and S_{IC} , of the two phases, but we find no strong evidence for this. Additionally, given that the sample has multivalent Mn, magnetic phase segregation would probably correspond to segregation of Mn^{3+} and Mn^{4+} which would be identifiable from structural analysis (as would the corresponding change in local K^+ content). We therefore consider it likely that both IRs coexist over the bulk of the sample. Fixing the scale factors $S_C = S_{\text{IC}} = S_{\text{crystal}}$ the refinement determines

the magnitude of each moment at 47 K for the commensurate component to be $0.297(2) \mu_B$, and the magnitude of the individual moments in the incommensurate component (assuming purely helical modulation) to be $0.502(4) \mu_B$. The net magnitude of each individual moment would result from the superposition of the commensurate and incommensurate components; at 47 K, the magnitude for each moment occurs in the range $0.502(4) \pm 0.297(2) \mu_B$. We note here that at 47 K the magnetization is far from being saturated as can be clearly seen from Figure 3(a), which is why the moment magnitudes are smaller than the fully saturated moments expected for $\text{Mn}^{3+}/\text{Mn}^{4+}$. The obtained moment from the commensurate component is approximately consistent with that obtained from the fixed-temperature, variable-field measurement [Figure 5].

We note that we observe no temperature-dependence in the value of k_z in the incommensurate $\vec{k}_{\text{mag}} = (0, 0, k_z)$ magnetic component between 40 K and 47 K. However, as noted above, there are changes to the spin-orientation of the commensurate phase on cooling between T_2 and T_3 .

Neutron diffraction: $T < T_3$

For $T < T_3$ we only have one diffraction pattern, at 2.5 K. There are many more peaks in the 2.5 K-60 K difference pattern than in the 47 K-60 K difference pattern, although the peaks due to the $\vec{k}_{\text{mag}} = (0, 0, \sim 0.37)$ component disappear entirely (see Figure 6). This increase in the number of peaks is in part due to the magnetic ordering of Mn_3O_4 , which exhibits several additional magnetic peaks due to its commensurate magnetic structure below ~ 33 K.²⁵⁻²⁸ Despite this, most of the peaks are not attributable to a known impurity and are therefore attributed to cryptomelane. It should be noted here that it has been reported that at low-temperatures, Mn_3O_4 exhibits some structural phase separation, with a fraction of it exhibiting an orthorhombic structure as opposed to its usual tetragonal structure;^{28,56,57} however, such effects are too subtle to observe when Mn_3O_4 is a minor impurity, and we do not include the reported orthorhombic phase in our analysis.

As previously stated, we do not see any structural transitions in $\text{K}_{1.461(4)}\text{Mn}_8\text{O}_{16}$, either from this neutron data or from low-temperature XRD (see Section IV of Supplementary Information). Additionally, the peaks in the neutron diffraction difference pattern 2.5 K-60 K are not present in the XRD down to 12 K, which is significant as neutrons scatter from spin density but x-rays do not. We can therefore be confident that these peaks are all magnetic in origin.

Similarly to $T_3 < T < T_2$, the majority of the magnetic peaks for $T < T_3$ cannot be indexed to a commensurate magnetic unit cell. However, the nuclear [110] and [220] Bragg peaks do increase in intensity at 2.5 K compared with 60 K, and so it is likely that, as is the case for $T_3 < T < T_2$, there is a commensurate component to the magnetic ground state. Unlike the higher-temperature commensurate component, such a component cannot have a net moment, as inferred from the lack of hysteresis for $T < T_3$ from the fixed-temperature variable-field magnetisation measurements [Figure 5]. Excluding these commensurate peaks, the remaining peaks can only be indexed to magnetic propagation vectors which are incommensurate in 3 spatial dimensions. A second possibility to index these magnetic peaks consists in assuming the presence of n incommensurate propagation vectors, where $n > 1$. Both of these possibilities are difficult to test with neutron powder diffraction alone, and so single-crystal studies are required. Consequently, we are not able to solve the magnetic structure for $T < T_3$, but we can say that it is more complex than for $T_3 < T < T_2$ and that it has magnetic Bragg peaks not consistent with a spin-glass-like state.

Discussion

The bond lengths and angles pertinent to the magnetic structure are given in Table 1. For J_1 and J_2 interactions it is unlikely there is direct exchange given the large bond lengths relative to the Shannon radii⁵⁸ of Mn^{3+} and Mn^{4+} . Given the presence of both Mn^{3+} and Mn^{4+} , rationalizing the nature of the interactions using the Goodenough-Kanamori-

Anderson rules^{59–61} is non-trivial. This is further complicated by the possibility for double exchange; whilst the Mn-O-Mn angles deviate from 90° , double exchange has been discussed in other mixed valent materials with non- 90° M -O- M (M = transition metal) bond angles, such as rutile chains.⁶²

Our finding that the magnetic ordering length-scale is incommensurate with the lattice parameters in $\text{K}_{1.461(4)}\text{Mn}_8\text{O}_{16}$ is in keeping with prior literature for doped- and undoped- α - MnO_2 . While, to our knowledge, there have been no theoretical studies on K-doped α - MnO_2 , a theoretical study on the undoped variant using a Heisenberg model⁴ does indeed predict helical ordering. The prediction in the study⁴ requires the angle of helical rotation of spins per lattice parameter, ϕ , to meet the condition $\pi/2 < \phi < \pi$, which in our case it does not, as $\phi \approx 0.37\pi$. This, and the lack of dopants in the theoretical study, means that a direct comparison between our work and the study⁴ cannot be made, but in general the theoretical prediction of helical ordering is broadly consistent with our finding for $T_3 < T < T_2$ that there is modulated magnetic ordering.

There is also a strong correspondence between our work and the helical ferrimagnetism model proposed by Sato *et al.*^{16,17} for $\text{K}_{1.5}(\text{H}_3\text{O})_x\text{Mn}_8\text{O}_{16}$. In this model, there are modulated spin and charge behaviours with length-scales λ_m and λ_c respectively, along the crystallographic axis of the tunnels. The modulated charge behaviour is due to mixed valent $\text{Mn}^{3+}/\text{Mn}^{4+}$. When $\lambda_c/\lambda_m = n$ (n being any integer), there will be a slight net magnetic moment. It is argued that for $25 < T < 55$ K, n is an integer, and the transition at $T \approx 25$ K results in n no longer having an integer value, hence the lack of a net moment below this temperature. This model, for $T_3 < T < T_2$, would be best represented in terms of propagation vectors by a dual- \vec{k} model with $\vec{k}_{\text{mag}} = (0, 0, k_z)$ and $\vec{k}_{\text{mag}} = (0, 0, 0)$, which is precisely what we show. Assuming charge-ordering length $\lambda_c = 8c$, $\lambda_c/\lambda_m \approx 3$ for $k_z = 0.37$, which is precisely the condition they propose for a slight net magnetic moment. Additionally, our isothermal and variable-temperature DC susceptibility measurements resemble those reported.^{16,17} Our work therefore supports the helical ferrimagnetism model of Sato *et al.*^{16,17}

Theoretical works indicate the α -MnO₂ crystallographic motif may lead to spin-glass behaviour,³ and previous experimental works support the theory that T_3 may be a spin-glass-like transition.^{21,22} From our DC and AC susceptibility measurements, we see an FC/ZFC divergence which could support this, though we do not see a strong frequency-dependence to the magnetic behaviour [Figure 4]. However, the magnetic Bragg structure we see for $T < T_3$ is not consistent with spin-glass-like ordering, as spin-glasses do not exhibit magnetic Bragg peaks.⁶³ The proposed transition to a spin-glass-like state is therefore not evident from our data, and if it is present, it is constrained to be an extrinsic phenomenon: either a surface effect, or resulting from variation in K⁺ content across the bulk sample. The possibility that spin-glassiness is a surface phenomenon has been suggested for similar materials, including Na_{2-x}Mn₈O₁₆⁶ and Ba_{1+ δ} Mn₈O₁₆.⁶⁴ The second possibility that a spin-glass is caused by variations in local K⁺ content within some regions of the sample is also highly plausible; it is already known that spin-glass-like behaviour occurs for K _{x} Mn₈O₁₆ ($x < 1$),^{15,18,19} and it has also been shown that Sn-doping of α -MnO₂ results in spin-glass-like behaviour.² Theoretical works also show a spin-glass ground state exists within the phase space of J_1 , J_2 , and J_3 .³ Therefore, we suggest that our observed magnetic Bragg peaks for $T < T_3$ may be reconcilable with previous claims of spin-glassiness, but that such a spin-glass-like state is not the bulk ground state of K_{1.461(4)}Mn₈O₁₆.

Our findings of magnetic Bragg peaks in both temperature regimes is consistent with the only known previous neutron diffraction study on K_{1.72}Mn₈O₁₆.²³ However, the magnetic peak positions do not match those in this study, with the result that our magnetic structure solution is unlikely to be the structural solution for their reported data, although there is the possibility for a $\vec{k}_{\text{mag}} = (0, 0, 0)$ component from their data, as for ours. This indicates that there is a strong sample-dependence of the magnetic propagation vector(s), which should be studied further in future work.

Conclusion

We have shown that, for $\text{K}_x\text{Mn}_8\text{O}_{16}$ with $x = 1.461(4)$, there are two distinct ordered magnetic structures in the temperature ranges $T < 24\text{ K}$ and $24 < T(\text{K}) < 54.5$. For $T < 24\text{ K}$, the sample has bulk magnetic ordering, so any spin-glass component in the sample is either due to surface effects or is a local phenomenon within some regions of the sample. For $24 < T < 54.5\text{ K}$, there is an incommensurate propagation vector $\vec{k}_{\text{mag}} = (0, 0, k_z)$ [$k_z = 0.36902(15)$], which is likely helical in the ab -plane, along with a commensurate magnetic cell which we successfully fit with a $\vec{k}_{\text{mag}} = (0, 0, 0)$ propagation vector with a spin canting in the $[110]$ direction. We contend that this is the helical ferrimagnetism model proposed in previous works.^{16,17}

Future work would consist of a single-crystal magnetic neutron study on cryptomelane to attempt to identify the nature of the magnetic ordering below 24 K , and to attempt to distinguish between helical, sinusoidal, and conical magnetic modulations for the incommensurate component of the magnetic structure. Additionally, neutron studies for a range of K^+ stoichiometries would be interesting, particularly to look at the different magnetic structure for $x < 1$ in $\text{K}_x\text{Mn}_8\text{O}_{16}$.

Acknowledgments

LNC and NDK acknowledge a scholarship EP/R513180/1 to pursue doctoral research from the UK Engineering and Physical Sciences Research Council (EPSRC). KS acknowledges funding from the British Council's Newton-Bhabha Fund PhD Placements Programme, which enabled him to visit the University of Cambridge on a research placement. JDB acknowledges support from the Faraday Institution (FIRG016). PB is grateful to Alexander von Humboldt Foundation (Bonn, Germany) for a 2022 Humboldt fellowship for experienced researchers. SED acknowledges funding from EPSRC (EP/T0285580/1).

Magnetic and heat capacity measurements at the University of Cambridge were made on

the EPSRC Advanced Characterization Suite (funded under EP/M0005/24/1). We acknowledge Diamond Light Source for time on the I11 instrument under BAG proposal CY28349. We acknowledge the Institut Laue-Langevin (ILL) for neutron diffraction measurements on the D20 and D2B instruments under proposal EASY-893.

LNC thanks Dr Chloe S. Coates for advice on analysing the synchrotron data, and Dr Saptarshi Mandal and Dr Efrain E. Rodriguez for useful correspondence.

We thank the following who made comments on the draft manuscript: Kavin Arunasalam, Dr Venkateswarlu Daramalla, Dr Farheen N. Sayed, and Adam J. Lovett.

Data availability

The variable-temperature neutron diffraction data from the ILL is available at doi:10.5291/ILL-DATA.EASY-893.⁶⁵ The remaining data is available in the University of Cambridge repository at doi:[XXXXXXXXXXXXXXXXXXXXXXXXXXXX].

Supplementary Information

A document containing Supplementary Information to this article is available [Link to PDF here].

References

- (1) Byström, A.; Byström, A. M. The crystal structure of hollandite, the related manganese oxide minerals, and α -MnO₂. *Acta Crystallographica* **1950**, *3*, 146–154.
- (2) Liu, X.; Xie, Y.; Hu, Z.; Lin, H.-J.; Chen, C.-T.; Dong, L.; Wang, Q.; Luo, S.-H., et al. Tuning the structural stability and spin-glass behavior in the α -MnO₂ nanotubes by Sn ions doping. *Phys. Chem. Chem. Phys.* **2022**, *24*, 12300–12310.

- (3) Crespo, Y.; Andrianov, A.; Seriani, N. Competing antiferromagnetic and spin-glass phases in a hollandite structure. *Physical Review B* **2013**, *88*, 014202.
- (4) Mandal, S.; Andrianov, A.; Crespo, Y.; Seriani, N. Incommensurate helical spin ground states on the hollandite lattice. *Physical Review B* **2014**, *90*, 104420.
- (5) Richmond, W. E.; Fleischer, M. Cryptomelane, a new name for the commonest of the “psilomelane” minerals. *American Mineralogist: Journal of Earth and Planetary Materials* **1942**, *27*, 607–610.
- (6) Lan, C.; Gong, J.; Liu, S.; Yang, S. Synthesis and magnetic properties of single-crystalline $\text{Na}_{2-x}\text{Mn}_8\text{O}_{16}$ nanorods. *Nanoscale Research Letters* **2011**, *6*, 133.
- (7) Poyraz, A. S.; Huang, J.; Pelliccione, C. J.; Tong, X.; Cheng, S.; Wu, L.; Zhu, Y.; Marschilok, A. C.; Takeuchi, K. J.; Takeuchi, E. S. Synthesis of cryptomelane type $\alpha\text{-MnO}_2(\text{K}_x\text{Mn}_8\text{O}_{16})$ cathode materials with tunable K^+ content: the role of tunnel cation concentration on electrochemistry. *Journal of Materials Chemistry A* **2017**, *5*, 16914–16928.
- (8) Chong, S.; Wu, Y.; Liu, C.; Chen, Y.; Guo, S.; Liu, Y.; Cao, G. Cryptomelane-type MnO_2 /carbon nanotube hybrids as bifunctional electrode material for high capacity potassium-ion full batteries. *Nano Energy* **2018**, *54*, 106–115.
- (9) Sada, K.; Senthilkumar, B.; Barpanda, P. Cryptomelane $\text{K}_{1.33}\text{Mn}_8\text{O}_{16}$ as a cathode for rechargeable aqueous zinc-ion batteries. *Journal of Materials Chemistry A* **2019**, *7*, 23981–23988.
- (10) Luo, J.; Zhang, Q.; Garcia-Martinez, J.; Suib, S. L. Adsorptive and acidic properties, reversible lattice oxygen evolution, and catalytic mechanism of cryptomelane-type manganese oxides as oxidation catalysts. *Journal of the American Chemical Society* **2008**, *130*, 3198–3207.

- (11) Santos, V. P.; Bastos, S. S. T.; Pereira, M. F. R.; Órfão, J. J. M.; Figueiredo, J. L. Stability of a cryptomelane catalyst in the oxidation of toluene. *Catalysis Today* **2010**, *154*, 308–311.
- (12) Santos, V. P.; Pereira, M. F. R.; Órfão, J. J. M.; Figueiredo, J. L. Mixture effects during the oxidation of toluene, ethyl acetate and ethanol over a cryptomelane catalyst. *Journal of Hazardous Materials* **2011**, *185*, 1236–1240.
- (13) Davó-Quñonero, A.; Navlani-García, M.; Lozano-Castello, D.; Bueno-López, A. CuO/cryptomelane catalyst for preferential oxidation of CO in the presence of H₂: deactivation and regeneration. *Catalysis Science & Technology* **2016**, *6*, 5684–5692.
- (14) Strobel, P.; Vicat, J.; Qui, D. T. Thermal and physical properties of hollandite-type K_{1.3}Mn₈O₁₆ and (K, H₃O)_xMn₈O₁₆. *Journal of Solid State Chemistry* **1984**, *55*, 67–73.
- (15) Suib, S. L.; Iton, L. E. Magnetic studies of manganese oxide octahedral molecular sieves: a new class of spin glasses. *Chemistry of Materials* **1994**, *6*, 429–433.
- (16) Sato, H.; Yamaura, J.-I.; Enoki, T.; Yamamoto, N. Magnetism and electron transport phenomena of manganese oxide ion exchanger with tunnel structure. *Journal of Alloys and Compounds* **1997**, *262*, 443–449.
- (17) Sato, H.; Enoki, T.; Yamaura, J.-I.; Yamamoto, N. Charge localization and successive magnetic phase transitions of mixed-valence manganese oxides K_{1.5}(H₃O)_xMn₈O₁₆ (0 < x < 0.5). *Physical Review B* **1999**, *59*, 12836.
- (18) Luo, J.; Zhu, H.; Zhang, F.; Liang, J.; Rao, G.; Li, J.; Du, Z. Spin-glass like behavior of K⁺-containing α-MnO₂ nanotubes. *Journal of Applied Physics* **2009**, *105*, 093925.
- (19) Luo, J.; Zhu, H.; Liang, J.; Rao, G.; Li, J.; Du, Z. Tuning magnetic properties of α-MnO₂ nanotubes by K⁺ doping. *The Journal of Physical Chemistry C* **2010**, *114*, 8782–8786.

- (20) Tseng, L.-T.; Lu, Y.; Fan, H. M.; Wang, Y.; Luo, X.; Liu, T.; Munroe, P.; Li, S.; Yi, J. Magnetic properties in α -MnO₂ doped with alkaline elements. *Scientific Reports* **2015**, *5*, 9094.
- (21) Barudžija, T.; Kusigerski, V.; Cvjetičanin, N.; Šorgić, S.; Perović, M.; Mitrić, M. Structural and magnetic properties of hydrothermally synthesized β -MnO₂ and α -K_xMnO₂ nanorods. *Journal of Alloys and Compounds* **2016**, *665*, 261–270.
- (22) Barudžija, T.; Perović, M.; Bošković, M.; Cvjetičanin, N.; Gyergyek, S.; Mitrić, M. Magnetic memory effect in hollandite-type α -K_xMnO₂ monocrystalline nanorods. *Journal of Alloys and Compounds* **2020**, *820*, 153406.
- (23) Larson, A. M. Frustrated Magnetism and Electronic Properties of Hollandite Oxide Materials (Chapter 4). Ph.D. thesis, University of Maryland, 2017.
- (24) Larson, A. M.; Moetakef, P.; Gaskell, K.; Brown, C. M.; King, G.; Rodriguez, E. E. Inducing ferrimagnetism in insulating hollandite Ba_{1.2}Mn₈O₁₆. *Chemistry of Materials* **2015**, *27*, 515–525.
- (25) Boucher, B.; Buhl, R.; Perrin, M. Magnetic structure of Mn₃O₄ by neutron diffraction. *Journal of Applied Physics* **1971**, *42*, 1615–1617.
- (26) Boucher, B.; Buhl, R.; Perrin, M. Propriétés et structure magnétique de Mn₃O₄. *Journal of Physics and Chemistry of Solids* **1971**, *32*, 2429–2437.
- (27) Jensen, G. B.; Nielsen, O. V. The magnetic structure of Mn₃O₄ Hausmannite between 4.7 K and Neel point, 41 K. *Journal of Physics C: Solid State Physics* **1974**, *7*, 409–424.
- (28) Kemei, M. C.; Harada, J. K.; Seshadri, R.; Suchomel, M. R. Structural change and phase coexistence upon magnetic ordering in the magnetodielectric spinel Mn₃O₄. *Physical Review B* **2014**, *90*, 064418.

- (29) Melot, B. C.; Tackett, R.; O'Brien, J.; Hector, A. L.; Lawes, G.; Seshadri, R.; Ramirez, A. P. Large low-temperature specific heat in pyrochlore $\text{Bi}_2\text{Ti}_2\text{O}_7$. *Physical Review B* **2009**, *79*, 224111.
- (30) Mukherjee, P.; Dutton, S. E. Enhanced magnetocaloric effect from Cr substitution in Ising lanthanide gallium garnets $\text{Ln}_3\text{CrGa}_4\text{O}_{12}$ (Ln= Tb, Dy, Ho). *Advanced Functional Materials* **2017**, *27*, 1701950.
- (31) Kelly, N. D.; Liu, C.; Dutton, S. E. Structure and magnetism of a new hexagonal polymorph of $\text{Ba}_3\text{Tb}(\text{BO}_3)_3$ with a quasi-2D triangular lattice. *Journal of Solid State Chemistry* **2020**, *292*, 121640.
- (32) Kelly, N. D.; Yuan, L.; Pearson, R. L.; Suard, E.; Orench, I. P.; Dutton, S. E. Magnetism on the stretched diamond lattice in lanthanide orthotantalates. *Physical Review Materials* **2022**, *6*, 044410.
- (33) Koskelo, E. C.; Liu, C.; Mukherjee, P.; Kelly, N. D.; Dutton, S. E. Free-Spin Dominated Magnetocaloric Effect in Dense Gd^{3+} Double Perovskites. *Chemistry of Materials* **2022**, *34*, 3440–3450.
- (34) Smith, D. R.; Fickett, F. R. Low-temperature properties of silver. *Journal of Research of the National Institute of Standards and Technology* **1995**, *100*, 119–171.
- (35) Debye, P. Zur theorie der spezifischen wärmen. *Annalen der Physik* **1912**, *344*, 789–839.
- (36) Thompson, S. P.; Parker, J. E.; Potter, J.; Hill, T. P.; Birt, A.; Cobb, T. M.; Yuan, F.; Tang, C. C. Beamline I11 at Diamond: A new instrument for high resolution powder diffraction. *Review of Scientific Instruments* **2009**, *80*, 075107.
- (37) Thompson, S. P.; Parker, J. E.; Marchal, J.; Potter, J.; Birt, A.; Yuan, F.; Fearn, R. D.; Lennie, A. R.; Street, S. R.; Tang, C. C. Fast X-ray powder diffraction on I11 at Diamond. *Journal of Synchrotron Radiation* **2011**, *18*, 637–648.

- (38) Coelho, A. A. TOPAS and TOPAS-Academic: an optimization program integrating computer algebra and crystallographic objects written in C++. *Journal of Applied Crystallography* **2018**, *51*, 210–218.
- (39) Rietveld, H. A profile refinement method for nuclear and magnetic structures. *Journal of Applied Crystallography* **1969**, *2*, 65–71.
- (40) Thompson, P.; Cox, D. E.; Hastings, J. B. Rietveld refinement of Debye-Scherrer synchrotron X-ray data from Al₂O₃. *Journal of Applied Crystallography* **1987**, *20*, 79–83.
- (41) Stephens, P. W. Phenomenological model of anisotropic peak broadening in powder diffraction. *Journal of Applied Crystallography* **1999**, *32*, 281–289.
- (42) Peterse, W. J.; Palm, J. H. The anisotropic temperature factor of atoms in special positions. *Acta Crystallographica* **1966**, *20*, 147–150.
- (43) Rodríguez-Carvajal, J. FullProf. *CEA/Saclay, France* **2001**,
- (44) Richard, D.; Ferrand, M.; Kearley, G. J. Analysis and visualisation of neutron-scattering data. *Journal of Neutron Research* **1996**, *4*, 33–39.
- (45) Le Bail, A.; Duroy, H.; Fourquet, J. L. Ab-initio structure determination of LiSbWO₆ by X-ray powder diffraction. *Materials Research Bulletin* **1988**, *23*, 447–452.
- (46) Rodríguez-Carvajal, J. A program for calculating irreducible representation of little groups and basis functions of polar and axial vector properties. *Program included Full-Prof Suite, version July-2010, ILL* **2010**,
- (47) Ritter, C. Neutrons not entitled to retire at the age of 60: More than ever needed to reveal magnetic structures. **2011**, *170*, 263–269.
- (48) Dollase, W. A. Correction of intensities for preferred orientation in powder diffractometry: application of the March model. *Journal of Applied Crystallography* **1986**, *19*, 267–272.

- (49) Vicat, J.; Fanchon, E.; Strobel, P.; Tran Qui, D. The structure of $K_{1.33}Mn_8O_{16}$ and cation ordering in hollandite-type structures. *Acta Crystallographica Section B: Structural Science* **1986**, *42*, 162–167.
- (50) Rodriguez-Carvajal, J.; Hennion, M.; Moussa, F.; Moudden, A. H.; Pinsard, L.; Revcolevschi, A. Neutron-diffraction study of the Jahn-Teller transition in stoichiometric $LaMnO_3$. *Physical Review B* **1998**, *57*, R3189.
- (51) Baur, W. H. The geometry of polyhedral distortions. Predictive relationships for the phosphate group. *Acta Crystallographica Section B: Structural Crystallography and Crystal Chemistry* **1974**, *30*, 1195–1215.
- (52) Lawler, K. V.; Smith, D.; Evans, S. R.; Dos Santos, A. M.; Molaison, J. J.; Bos, J.-W. G.; Mutka, H.; Henry, P. F.; Argyriou, D. N.; Salamat, A., et al. Decoupling Lattice and Magnetic Instabilities in Frustrated $CuMnO_2$. *Inorganic Chemistry* **2021**, *60*, 6004–6015.
- (53) Kimber, S. A. J. Charge and orbital order in frustrated $Pb_3Mn_7O_{15}$. *Journal of Physics: Condensed Matter* **2012**, *24*, 186002.
- (54) Nagle-Cocco, L. A. V.; Bull, C. L.; Ridley, C. J.; Dutton, S. E. Pressure Tuning the Jahn-Teller Transition Temperature in $NaNiO_2$. *ACS Inorganic Chemistry* **2022**, *61*, 4312–4321.
- (55) Drits, V. A.; Silvester, E.; Gorshkov, A. I.; Manceau, A. Structure of synthetic monoclinic Na-rich birnessite and hexagonal birnessite: I. Results from X-ray diffraction and selected-area electron diffraction. *American Mineralogist* **1997**, *82*, 946–961.
- (56) Kim, M.; Chen, X. M.; Wang, X.; Nelson, C. S.; Budakian, R.; Abbamonte, P.; Cooper, S. L. Pressure and field tuning the magnetostructural phases of Mn_3O_4 : Raman scattering and x-ray diffraction studies. *Physical Review B* **2011**, *84*, 174424.

- (57) Chung, J.-H.; Hwan Lee, K.; Song, Y.-S.; Suzuki, T.; Katsufuji, T. Low temperature structural instability of tetragonal spinel Mn_3O_4 . *Journal of the Physical Society of Japan* **2013**, *82*, 034707.
- (58) Shannon, R. D.; Prewitt, C. T. Revised values of effective ionic radii. *Acta Crystallographica Section B: Structural Crystallography and Crystal Chemistry* **1970**, *26*, 1046–1048.
- (59) Goodenough, J. B. Theory of the role of covalence in the perovskite-type manganites $[\text{La}, \text{M(II)}]\text{MnO}_3$. *Physical Review* **1955**, *100*, 564.
- (60) Goodenough, J. B. An interpretation of the magnetic properties of the perovskite-type mixed crystals $\text{La}_{1-x}\text{Sr}_x\text{CoO}_{3-\lambda}$. *Journal of Physics and Chemistry of Solids* **1958**, *6*, 287–297.
- (61) Kanamori, J. Superexchange interaction and symmetry properties of electron orbitals. *Journal of Physics and Chemistry of Solids* **1959**, *10*, 87–98.
- (62) Dutton, S. E.; Hanson, E. D.; Broholm, C. L.; Slusky, J. S.; Cava, R. J. Magnetic properties of hole-doped SCGO, $\text{SrCr}_8\text{Ga}_{4-x}\text{M}_x\text{O}_{19}$ ($\text{M} = \text{Zn}, \text{Mg}, \text{Cu}$). *Journal of Physics: Condensed Matter* **2011**, *23*, 386001.
- (63) Binder, K.; Young, A. P. Spin glasses: Experimental facts, theoretical concepts, and open questions. *Reviews of Modern physics* **1986**, *58*, 801–976.
- (64) Yu, J.; Tang, S.; Wang, L.; Du, Y. Spin-glass-like behavior in hollandite $\text{Ba}_{1+\delta}\text{Mn}_8\text{O}_{16}$ nanoribbons synthesized by molten-salt method. *Chemical Physics Letters* **2010**, *496*, 117–121.
- (65) Liam A. V. Nagle-Cocco and E. Suard. Elucidating the origin of the magnetic behaviour of cathode material $\text{K}_{1.33}\text{Mn}_8\text{O}_{16}$. Institut Laue-Langevin. doi:10.5291/ILL-DATA.EASY-893. 2021; <https://data.isis.stfc.ac.uk/doi/STUDY/113601628/>.